

Electronic instabilities in Penrose quasi-crystals: competition, coexistence and collaboration of order

J.B. Profe,¹ C. Honerkamp,^{1,2} S. Achilles,^{3,4} and D.M. Kennes^{5,6}

¹*Institute for Theoretical Solid State Physics, RWTH Aachen University, 52074 Aachen, Germany*

²*JARA-FIT, Jülich Aachen Research Alliance - Fundamentals of Future Information Technology, Germany*

³*Jülich Supercomputing Centre, Forschungszentrum Jülich, Wilhelm-Johnen-Straße, 52425 Jülich, Germany*

⁴*RWTH Aachen University, Aachen Institute for Advanced Study in*

Computational Engineering Science, Schinkelstr. 2, 52062 Aachen, Germany

⁵*Institut für Theorie der Statistischen Physik, RWTH Aachen, 52074 Aachen,*

Germany and JARA - Fundamentals of Future Information Technology

⁶*Max Planck Institute for the Structure and Dynamics of Matter and*

Center for Free Electron Laser Science, 22761 Hamburg, Germany

(Dated: September 21, 2024)

Quasi-crystals lack translational symmetry, but can exhibit long-ranged order, a phenomenon well understood in crystals with translational symmetry. We develop a functional renormalization group approach in two-dimensional real space and apply it to interacting electrons on quasi-crystalline lattices. Thereby, we treat competing electronic instabilities in an unbiased, beyond-mean-field approach. The formalism is presented in general and applied to the prototypical Penrose lattice Hubbard model, which is found to exhibit a delicate interplay between charge and spin degrees of freedom. Depending on the range of interactions and hopping amplitudes in the Penrose lattice, we unveil a rich phase diagram including antiferromagnetic orderings, charge density waves and subleading, superconducting pairing tendencies. Surprisingly, these phases can coexist in a spatially separated fashion, compete or mutually collaborate depending on the model parameters. This reveals 'the tip of an iceberg' of an even richer playground for electronic interaction effects in such quasi-crystalline systems. It also renders an unbiased, beyond-mean-field approach, such as the developed functional renormalization group scheme, essential to correctly capture the physics at play.

Introduction. — Since the discovery of quasi-crystals, there has been exciting experimental [1–7] and theoretical [8–11] research on the topic. Recently, reports of superconductivity [12] as well as antiferromagnetic ordering [13] in quasi-crystalline systems (and their approximants, which are large clusters of quasi-crystalline tilings as periodically repeated unit cells) opened a gap between our theoretical understanding and experimental results. For theory, an intrinsic complication in these systems is the non-layered structure in three dimensions (3D). An exception to this are twisted materials, like twisted bilayer graphene, which form quasi-crystals for a variety of incommensurable twisting angles [5]. More fundamentally, the lack of translational symmetry in quasi-crystals leads to a loss of momentum conservation resulting in severe computational challenges.

A much-studied example of a quasi-periodic two-dimensional (2D) structure is the Penrose tiling [14]. It has a five-fold rotational symmetry and can be seen as the 2D cut through an icosahedral quasi-crystal [1]. It constitutes a prototypical model to understand many phenomena in quasi-crystalline materials, e.g., being currently used to investigate the experimentally observed superconductivity [15–18]. Explanations include the existence of unconventional superconductivity generated by fluctuations. However, the mean-field theory employed in these studies is biased due to the choice of the decoupling and it remains unclear whether other orderings might pre-

vail. Thus, we are in clear demand of an unbiased, beyond mean-field method to explore the physics of quasi-crystals. Available beyond mean-field methods for quasi-crystals are, however, limited as the thermodynamic limit requires large lattice sizes, ruling out many simulation techniques, such as exact diagonalization. Tensor network based approaches are hampered by the excessive growth of entanglement in these systems [19]. The sign problem rules out quantum Monte-Carlo [20] simulations for large regimes of the parameter space [21].

In this letter, we provide such an unbiased approach by putting forward a functional renormalization group (FRG) [22] based, real-space equivalent of the truncated unity FRG (TU-FRG) [23]. This method can be applied to a plethora of problems in which the translation symmetry is broken such as quasi-crystals, but also spatial boundaries or impurities, for example. We then employ the developed method to unveil a rich phase-diagram of the Penrose model. We find a charge-ordered phase to emerge upon including nearest-neighbor interactions. This results in a remarkable interplay between charge and spin order, leading either to a mutual suppression or a mutual spatial evasion of phases depending on the type of Penrose model. Furthermore, for exponentially decaying hoppings in space we find that several ordering tendencies collaborate revealing the intricate nature of ordering tendencies in quasi-crystals. This unveils that to correctly capture the in general intricate nature of

orderings in quasi crystals requires an unbiased, beyond-mean-field approach, such as the one presented in this letter.

Model and Method. — The Penrose tiling we examine is generated by the substitution method [24] using 10 triangles as the initial configuration. Based on this tiling, we construct Hubbard models with sites located on either the vertices or the centers of the rhombi of the lattice, called vertex-type or center-type models, respectively (compare Fig. 1). In all simulations presented here, we use 3126 lattice sites in the vertex model or 3010 in the center model, but we checked that the phases and critical scales do not change significantly upon further increasing the lattice size. The Hamiltonian in second quantization reads

$$H = - \sum_{i,j,\sigma} (t_{i,j} + \mu\delta_{i,j}) c_{i,\sigma}^\dagger c_{j,\sigma} + \frac{1}{2} \sum_{i,\sigma,\sigma'} U n_{i,\sigma} n_{i,\sigma'} + \frac{1}{2} \sum_{\langle i,j \rangle, \sigma, \sigma'} U' n_{i,\sigma} n_{j,\sigma'} . \quad (1)$$

with the operators $c_{i,\sigma}^{(\dagger)}$ annihilating (creating) an electron on site i with spin σ . We concentrate on two cases for the hopping amplitudes. First, we apply nearest-neighbor hoppings for which the first sum in Eq. (1) is restricted to pairs $\langle i, j \rangle$ denoting neighboring sites with $t_{i,j} = t_0$ as shown as red lines in Fig. 1 (see supplementary material (SM) [25]). Secondly, we also consider exponentially decaying hoppings using an exponential form $t_{i,j} = t_0 e^{1 - \frac{|r_i - r_j|}{a}}$. Here, r_i is the real space position of the site i . We choose the minimal distance of any two sites, $a = \min_{i,j} |r_i - r_j|$, as lattice spacing and measure bond lengths relative to it [16]. For convenience, we set the unit $t_0 = 1$. We assume spin-independence of the interaction with an on-site repulsion U and a nearest-neighbor repulsion U' , resulting in an SU(2)-symmetric Hamiltonian. This is a convenient, but in no means necessary, simplification for our approach (see [25]).

To treat possible competing orders in an unbiased fashion, we employ a real-space variant of the so-called TU-FRG [23, 26, 27], based on a one-loop formulation of the FRG [22, 28]. In an FRG scheme, a cutoff function Λ is introduced in the bare propagator, such that the system reduces to a solvable problem at an initial scale. At a final scale, the full solution is recovered. By variations of the cutoff parameter, one obtains an infinite set of flow (differential) equations. This set of flow equations needs to be truncated in order to be numerically tractable, lending the FRG a perturbative character, albeit to infinite order. Here, we employ one of the most commonly applied truncations, keeping only the effective two-particle interaction. We additionally neglect the bosonic frequency dependence of the effective two-particle interaction. Both are common, successful approximations in 2D in the study of competing instabil-

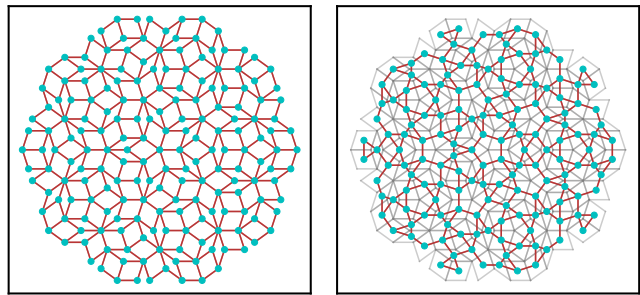


FIG. 1: Four times iterated Penrose tiling with the vertex-type left and the center-type right. Nearest neighbors are marked as red bonds. The rhombi referred to in the main text are shown in grey for the center tiling.

ities in crystalline structures [22, 29–31]. The terms in the effective interaction can be grouped in three channels, lending them physical interpretations relating each to a separate fermionic bilinear [22] and a certain effective mean-field Hamiltonian. Thus, a divergence (also called flow to strong coupling) in a certain channel can be directly associated with an emergent order parameter and possibly to a gap opening in the corresponding mean-field picture, indicative of a phase transition. The spatial structure of the gap function as a measurable quantity is encoded in the type and strength of the fermionic bilinear coupling that flows to large values. More specifically, we have the P -channel to indicate a pairing gap opening, the C -channel for magnetic order and the D -channel for emergent charge order (see [25]). In practice, the spatial ordering information is extracted from the leading eigenvectors of the diverging channel. In doing so we can predict the energy gap up to an unknown prefactor. As we do not account for self-energy feedback (gap opening) we are not able to flow into the symmetry-broken phase. Thus, we stop the flow if an eigenvalue of one of the three channels surpasses a threshold corresponding to the stopping scale denoted as $\Lambda = \Lambda_C$.

Competing Orders in Vertex-Type Penrose Model. — First, we investigate the vertex model including nearest-neighbor hopping at half filling. The model is bipartite and known to show antiferromagnetic ordering in the case of $U' = 0$ and $U > 0$ [21, 32]. The density of states (DoS) has a δ -like peak at $\omega = 0.0$ with a small gap right next to it (see [25]). This peak does not arise due to a Van-Hove singularity (which are very relevant in the context of ordering in crystals), but instead occurs due to a macroscopic number of degenerate states with eigenvalue zero [33–35].

Considering first half-filling ($\mu = 0.0$) and temperature $T = 10^{-3}$ reveals a delicate dependence of the order on the edges of the Penrose lattice in the (U, U') -plane with strongly pronounced edge ordering tendencies. However,

such finite size effects (although perfectly physical and within the capabilities of our real-space approach) are not the main concern of our analysis, which focuses on the bulk properties. We therefore choose to screen the interaction strength towards the edge of the system employing a tanh envelope (see [25]). However, as we demonstrate in the SM [25] except for slight quantitative changes, the bulk phase diagram looks the same as discussed below for the screened case.

In the main panel of Fig. 2 we summarize the phase diagram of the vertex-type Penrose lattice. For $U \gg U'$ (lower right part of the phase diagram), the antiferromagnetic spin-density wave (SDW) instability prevails similar to the one at half-filling without nearest-neighbor interactions ($U' = 0$). The corresponding order parameter is illustrated in the lower left inset. For increased U'/U , the leading divergence changes to a charge density wave (CDW) with order parameter as shown in the upper left inset. The leading eigenvector has a self-similar form and is non-degenerate. The transition between SDW and CDW is accompanied by a reduction of the critical scales. Without inter-channel coupling (which can be analyzed by turning off the feedback of one channel to another in our approach) the critical scale is $\Lambda_C \approx 0.4$ at the transition. In the simulation incorporating inter-channel feedback, this is reduced to $\Lambda_C \approx 0.17$. Thus, we conclude that ordering tendencies compete leading to a mutual suppression of the channels.

To sum up, the physics of the *vertex-type* Penrose model is similar to the one of crystals with translational invariance, where multiple mutually competing bulk orders take center stage. The quasi-crystal structure defines an atypical DoS, but nonetheless similarly competing orders as in the crystalline cases are unveiled here.

Spatial Coexistence of Order in the Center-Type Penrose Model. — Next, we examine a center-type Penrose model including nearest-neighbor hopping and interaction. This model is not bipartite and, in contrast to the vertex model, each site has the same coordination number, four. The DoS (see [25]) displays two main peaks consisting of a macroscopic number of degenerate states (as discussed above): one at $\omega \approx 2.35$ and one at $\omega = 2.0$. A fraction of the states contributing to the peak at $\omega = 2.0$ are so-called string states which are self-similar with a fractional dimension of 1.44 [9, 10].

We concentrate on Fermi levels at and around these main features and find a CDW as well as a SDW divergence depending on the values of U and U' . The string states support both, which leads to a competition of the D - and C -channel as above. Upon lowering or raising the chemical potential, moving away from the DoS peak, we suppress the influence of the string states. As a result of this, the CDW divergence is shifted to stronger nearest-neighbor interactions, whereas the SDW divergence persists, but the critical scales are reduced and the real space shape of the leading order changes (see [25]).

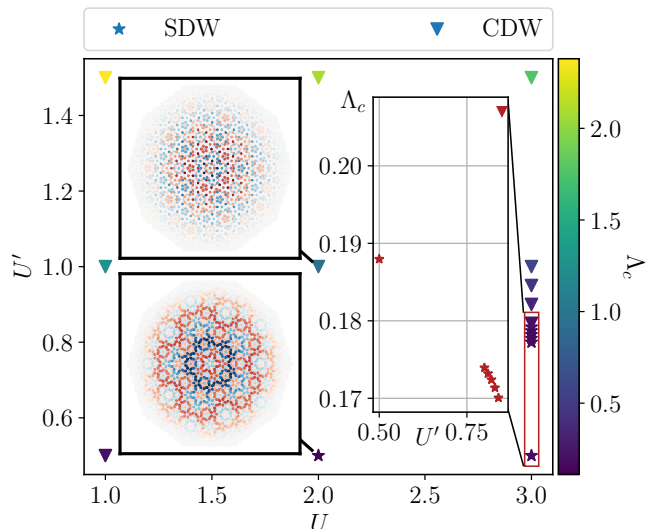


FIG. 2: Critical scales of CDW and SDW divergences at $\mu = 0.0$ and $T = 10^{-3}$ with screened interaction towards the boundaries. The upper left inset shows the charge order at $U' = 1.5$ and $U = 1$, the colormap is diverging so blue and red mark different signs. The lower left inset shows the spin order parameter (or magnetization pattern), at $U' = 0.5$ and $U = 2.0$. On the right side, the critical scales depending on the nearest-neighbor interaction are shown for $U = 3.0$, to highlight the suppression of the critical scale upon approaching the phase transition.

The region in which the transition between SDW and CDW occurs is of special interest to us. Again we find a slight reduction of the critical scales. But in contrast to the vertex model, the maximal two channels, namely C and D , diverge on equal footing. This competition is now realized in a way that the two orders coexist in a spatially separated fashion, opening gaps in different regions of the lattice. To show this more clearly, we proceed with a mean-field (MF) decoupling of the effective FRG vertex at the final scale Λ_C , (see [25, 36]). The spatially separated support of the non-zero gaps for charge and spin order are shown in Fig. 3. The spin order forms in the center as a self-similar star like structure. It shows short-ranged magnetic ordering with alternating sign on the half length-scale to the first self-similar feature. The charge order emerges close to the boundary of the system and has strongly peaked maximal values separated by an order of magnitude from the lower gap values. It forms 10 candy-cane like shaped islands with alternating sign between neighboring sites. In the transition region both have low weight. This behavior arises generically at low U and U' combinations close to the transition line between the charge and spin ordering. The ordering is quite sensitive to changes in U and U' , as moving away from the transition line rapidly promotes a single phase.

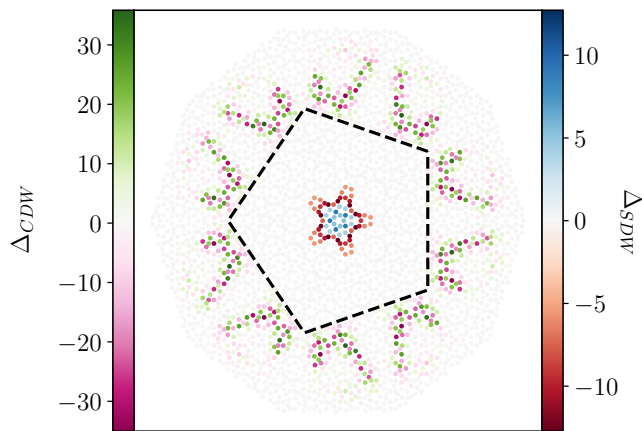


FIG. 3: Gap values of the decoupled effective interaction at Λ_C for $U = 0$, $U' = 0.3$ and $T = 10^{-3}$.

Leading eigenvalues of the D - and C -channel have approximately the same magnitude. The calculated gap magnitudes are shown in a red-blue color scheme for the spin gap which is equivalent to the magnetisation. In the pink-green color scheme the charge gap is shown. The two faces have no spatial overlap of magnitudes above $10^{-3}\max(\Delta)$. The inserted dashed pentagon indicates the separation of spin and charge region.

Due to the spatially separated nature, the two orders coexist without affecting each other.

Summarizing these findings, we have identified a co-occurrence of mutually evasive orders with clear spatial separation in the *center-type* Penrose model. Such instabilities can likely only be found in structures with (infinitely) large unit cells such as true quasi-crystals, their large-scale approximants or twisted moiré materials, which is a particularly rapidly developing field.

Collaborative Order in Physical Center-Type Penrose Model. — Finally, we investigate the phase-diagram of a center-type Penrose model with hopping amplitudes decaying exponentially in real space. For such models recently a unconventional superconducting order has been predicted [16]. The DoS in this setup has three main peaks at $\omega \approx 0.83, 0.99, 1.23$, (see [25]). The peaks arise partially due to degeneracy as well as partially due to a smaller slope of the dispersion in the eigenbasis of the Hamiltonian. Between the second and the third peak, there is a small energy gap. The most interesting physics is again expected for the Fermi level at the DoS peaks or in their vicinity. For the simulations we chose $U' = 0$. We again screen the interaction towards the edge as described for the vertex-type Penrose model.

We find a SDW to be the dominant phase in the whole interaction region at all three peaks of the DoS. The ordering pattern is dependent on the filling as well as the interaction strength (see [25]). Upon decreasing U to 0.3 we observe the emergence of a sub-leading pairing divergence

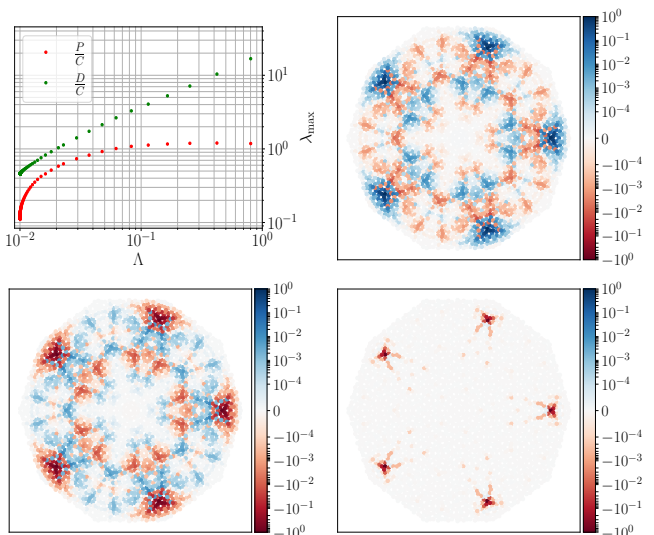


FIG. 4: Relative critical scales and leading eigenvectors of all three channels at $U = 0.3$, $\mu = 0.99$ and $T = 10^{-3}$ including all sites with a distance $\leq 3a$. Only the on-site component of the leading eigenvectors is shown as higher form-factor components are at least suppressed by a factor of 100 (see [25]). The upper left plot shows the maximal eigenvalues of P - and D -channel relative to the leading eigenvalue of the C -channel. At the critical scale all three channels diverge resulting in a slow decay of P/C . The C -channel ordering pattern is shown in the upper right plot, the D -channel is shown in the lower left and the P -channel leading eigenvector is shown in the lower right plot.

indicated by a slower decay of λ_P/λ_C than at higher interactions. This is accompanied by the loss of the standard behavior for an emergent dominant spin-spin interaction, namely that at the divergence $\lambda_D/\lambda_C = 1/2$ [22]. Instead we find that λ_D/λ_C is not a constant as expected, but decreases upon approaching the critical scale see Fig. 4. The divergences of the P - and D -channel are both driven by the C -channel. The two channels in turn decrease the critical scale via their feedback to the C -channel. Upon further decreasing U , the critical scale will become lower than the temperature such that no divergence is occurring anymore at detectable scales. By lowering the temperature to $T = 0$ and using a sharp frequency cutoff we found that at $U = 0.2$ the observed tri-divergence is present whereas at $U = 0.1$ it vanishes and we recover the standard spin-density wave behaviour. This divergence of all three channels with only slightly different critical exponents renders a Random Phase Approximation-MF highly biased as any MF gap would be stable in such an approach. Note that analogous multi-channel instabilities are known to signal non-trivial non-MF ground states in one-dimensional models for correlated fermions [37–39] and were argued to indicate Fermi surface trun-

cations in the two-dimensional Hubbard models [40–42]. Yet, in this as well as in our case, a proper classification of the true ground state needs further work. In any case, it is exciting to see that quasi-crystalline systems offer another playground to exhibit such physics at the frontier of our understanding.

To sum up, in the center-type Penrose model with *exponentially decaying hopping amplitudes* we find a delicate mutual collaboration of ordering tendencies, pointing to an unconventional ground state. Here MF decouplings are highly biased and the approach put forward here needs to be employed. Recent theoretical reports of superconductivity should therefore be taken with caution if they focus on one particular channel in a mean-field treatment [16].

Conclusions. — We used a newly developed real-space truncated-unity FRG formalism to study the effects of nearest-neighbor interaction in quasi-crystals. In these infinite size unit cells the spatial degree of freedom opens up even greater variety of competing instabilities, allowing for spatial coexistence, mutual evasion and joint instabilities. We expect similar findings for large but finite unit cell systems, with twisted van der Waals heterostructures as most prominent [43] but certainly not last example.

For theory, it would be desirable to keep even higher accuracy, e.g. by taking into account the self-energy effects [44] and the frequency dependence of the vertex [27, 45–47]. This would allow to include interactions mediated by phonons or photons and thus to study conventional superconductivity in quasi-crystals [15]. On the level of real materials the next step would be the development of a feasible beyond inter-orbital-bilinears [48] approach, combining the here derived realspace TU-FRG with the k -space TU-FRG[23]. With such a scheme 3D-quasi crystalline approximants can be addressed, opening the ground for predictions of phase-diagrams of real materials if combined with density functional theory inputs [49, 50].

We thank J. Ehrlich, L. Klebl and J. Beyer for fruitful discussions and D. Rohe and E. Di Napoli for the help in optimizing the framework. The Deutsche Forschungsgemeinschaft (DFG, German Research Foundation) is acknowledged for support through RTG 1995 and under Germany's Excellence Strategy - Cluster of Excellence Matter and Light for Quantum Computing (ML4Q) EXC 2004/1 - 390534769. We acknowledge support from the Max Planck-New York City Center for Non-Equilibrium Quantum Phenomena. Simulations were performed with computing resources granted by RWTH Aachen University under project rwth0545.

[1] L. A. Bursill and P. Ju Lin, Nature **316**, 50 (1985).

- [2] D. Shechtman, I. Blech, D. Gratias, and J. W. Cahn, Physical Review Letters **53**, 1951 (1984).
- [3] D. Shi, Z. Budrikis, A. Stein, S. A. Morley, P. D. Olmsted, G. Burnell, and C. H. Marrows, Nature Physics **14**, 309 (2018).
- [4] K. Deguchi, S. Matsukawa, N. K. Sato, T. Hattori, K. Ishida, H. Takakura, and T. Ishimasa, Nature Materials **11**, 1013 (2012).
- [5] W. Yao, E. Wang, C. Bao, Y. Zhang, K. Zhang, K. Bao, C. K. Chan, C. Chen, J. Avila, M. C. Asensio, J. Zhu, and S. Zhou, Proceedings of the National Academy of Sciences **115**, 6928 (2018).
- [6] B. Deng, B. Wang, N. Li, R. Li, Y. Wang, J. Tang, Q. Fu, Z. Tian, P. Gao, J. Xue, and H. Peng, ACS Nano **14**, 1656 (2020).
- [7] L. C. Collins, T. G. Witte, R. Silverman, D. B. Green, and K. K. Gomes, Nature Communications **8**, 15961 (2017).
- [8] W. Steurer, Acta Crystallographica Section A Foundations and Advances **74**, 1 (2018).
- [9] K. Inayoshi, Y. Murakami, and A. Koga, Journal of the Physical Society of Japan **89**, 064002 (2020), eprint: <https://doi.org/10.7566/JPSJ.89.064002>.
- [10] T. Fujiwara, M. Arai, T. Tokihiro, and M. Kohmoto, Physical Review B **37**, 2797 (1988).
- [11] P. Moon, M. Koshino, and Y.-W. Son, Physical Review B **99**, 165430 (2019).
- [12] K. Kamiya, T. Takeuchi, N. Kabeya, N. Wada, T. Ishimasa, A. Ochiai, K. Deguchi, K. Imura, and N. K. Sato, Nature Communications **9**, 154 (2018).
- [13] S. Yoshida, S. Suzuki, T. Yamada, T. Fujii, A. Ishikawa, and R. Tamura, Physical Review B **100**, 180409(R) (2019).
- [14] R. Penrose, The Mathematical Intelligencer **2**, 32 (1979).
- [15] R. N. Araújo and E. C. Andrade, Physical Review B **100**, 014510 (2019), arXiv: 1903.09635.
- [16] Y. Cao, Y. Zhang, Y.-B. Liu, C.-C. Liu, W.-Q. Chen, and F. Yang, Physical Review Letters **125**, 017002 (2020).
- [17] S. Sakai and R. Arita, Physical Review Research **1**, 022002 (2019).
- [18] R. Chen, D.-H. Xu, and B. Zhou, Physical Review B **100**, 115311 (2019), arXiv: 1907.05724.
- [19] U. Schollwoeck, Annals of Physics **326**, 96 (2011), arXiv: 1008.3477.
- [20] The vertex model is bipartite and therefore accessible by QMC at half filling, but it is questionable if a thermodynamic limit is reachable.
- [21] A. Jagannathan, A. Szallás, S. Wessel, and M. Duneau, Physical Review B **75**, 212407 (2007).
- [22] W. Metzner, M. Salmhofer, C. Honerkamp, V. Meden, and K. Schoenhammer, Reviews of Modern Physics **84**, 299 (2012), arXiv: 1105.5289.
- [23] J. Lichtenstein, D. S. d. l. Peña, D. Rohe, E. D. Napoli, C. Honerkamp, and S. A. Maier, Computer Physics Communications **213**, 100 (2017).
- [24] C. Goodman-Strauss, The Annals of Mathematics **147**, 181 (1998).
- [25] .
- [26] F. Bauer, J. Heyder, and J. von Delft, Physical Review B **89**, 045128 (2014).
- [27] L. Weidinger, F. Bauer, and J. von Delft, Physical Review B **95**, 035122 (2017), arXiv: 1609.07423.
- [28] M. Salmhofer and C. Honerkamp, Progress of Theoretical

- Physics **105**, 1 (2001).
- [29] C. Honerkamp, D. Rohe, S. Andergassen, and T. Enss, *Physical Review B* **70**, 235115 (2004), arXiv: cond-mat/0403633.
 - [30] C. Platt, W. Hanke, and R. Thomale, *Advances in Physics* **62**, 453 (2013), arXiv: 1310.6191.
 - [31] L. Klebl, D. M. Kennes, and C. Honerkamp, arXiv:2002.11030 [cond-mat] (2020), arXiv: 2002.11030.
 - [32] A. Koga and H. Tsunetsugu, *Physical Review B* **96**, 214402 (2017).
 - [33] M. Kohmoto and B. Sutherland, *Physical Review B* **34**, 3849 (1986).
 - [34] M. Kohmoto and B. Sutherland, *Physical Review Letters* **56**, 2740 (1986).
 - [35] E. Day-Roberts, R. M. Fernandes, and A. Kamenev, arXiv:2004.12291 [cond-mat] (2020), arXiv: 2004.12291.
 - [36] J. Reiss, D. Rohe, and W. Metzner, *Physical Review B* **75**, 075110 (2007).
 - [37] M. P. A. Fisher, arXiv:cond-mat/9806164 (1998), arXiv: cond-mat/9806164.
 - [38] H.-H. Lin, L. Balents, and M. P. A. Fisher, *Physical Review B* **58**, 1794 (1998).
 - [39] K. L. Hur and T. Maurice Rice, *Annals of Physics* **324**, 1452 (2009).
 - [40] N. Furukawa, T. M. Rice, and M. Salmhofer, *Physical Review Letters* **81**, 3195 (1998).
 - [41] A. Läuchli, C. Honerkamp, and T. M. Rice, *Physical Review Letters* **92**, 037006 (2004).
 - [42] C. Honerkamp, M. Salmhofer, N. Furukawa, and T. M. Rice, *Physical Review B* **63**, 035109 (2001).
 - [43] D. M. Kennes, M. Claassen, L. Xian, A. Georges, A. J. Millis, J. Hone, C. R. Dean, D. N. Basov, A. Pasupathy, and A. Rubio, *Moiré heterostructures: a condensed matter quantum simulator*, invited to *Nat Phys* (under Review).
 - [44] C. Hille, D. Rohe, C. Honerkamp, and S. Andergassen, *Physical Review Research* **2** (2020), 10.1103/physrevresearch.2.033068.
 - [45] N. Wentzell, G. Li, A. Tagliavini, C. Taranto, G. Rohringer, K. Held, A. Toschi, and S. Andergassen, *Physical Review B* **102** (2020), 10.1103/physrevb.102.085106.
 - [46] T. Reckling and C. Honerkamp, *Physical Review B* **98**, 085114 (2018), arXiv: 1803.08431.
 - [47] D. Vildardi, C. Taranto, and W. Metzner, *Phys. Rev. B* **96**, 235110 (2017).
 - [48] C. Honerkamp, *Physical Review B* **98**, 155132 (2018), arXiv: 1805.01669.
 - [49] P. Hohenberg and W. Kohn, *Physical Review* **136**, B864 (1964).
 - [50] W. Kohn and L. J. Sham, *Physical Review* **140**, A1133 (1965).
 - [51] C. Husemann and M. Salmhofer, *Physical Review B* **79**, 195125 (2009), arXiv: 0812.3824.

Supplemental Material

Derivation of the flow equations

We now sketch the derivation of the flow equations. The effective vertex can be separated in three different channels, each of them related to a specific fermionic bilinear [22]. A divergence of their eigenvalues indicates a flow to strong coupling, which in turn leads to the opening of a specific gap in the self-energy. The P -channel indicates pairing, the C -channel gives information of magnetic ordering tendencies, and charge ordering information is contained in the D -channel. Technically the charge ordering information has to be extracted from the physical charge channel [51], but if no other channels diverge, the ordering can be extracted directly from the D -channel. This can be seen by a mean-field decoupling in the three native channels. In general, we can write the effective two-particle interaction $\Gamma^{\Lambda,(4)}$ as

$$\Gamma^{\Lambda,(4)}(1, 2; 3, 4) = U(1, 2; 3, 4) + \overset{\text{Particle-Particle (PP)}}{\Phi^P(1, 2; 3, 4)} + \overset{\text{Direct Particle-Hole (PH)}}{\Phi^D(1, 2; 3, 4)} + \overset{\text{Exchange/Crossed PH}}{\Phi^C(1, 2; 3, 4)} . \quad (2)$$

Each number represents a multi-index consisting of orbital, spin and frequency index. We will use quoted numbers, or quoted indices, for all degrees of freedom which are summed. The flow equation for the effective Interaction can be separated in those three channels [23] as can be seen in Eq. (3a)-(3c). As all occurring quantities are Λ -dependent we will from now on leave out the subscript.

$$\frac{d\Phi^P(1, 2; 3, 4)}{d\Lambda} = \sum \Gamma(1, 2; 1', 2') (G(1', 3')S(2', 4')) \Gamma(3', 4'; 3, 4) \quad (3a)$$

$$\begin{aligned} \frac{d\Phi^C(1, 2; 3, 4)}{d\Lambda} = \sum \Gamma(1, 4'; 1', 4) (G(1', 3')S(2', 4')) \\ + S(1', 3')G(2', 4')) \Gamma(3', 2; 3, 2') \end{aligned} \quad (3b)$$

$$\begin{aligned} \frac{d\Phi^D(1, 2; 3, 4)}{d\Lambda} = \sum \Gamma(1, 3'; 3, 2') (G(1', 3')S(2', 4')) \\ + S(1', 3')G(2', 4')) \Gamma(4', 2; 1', 4) \end{aligned} \quad (3c)$$

We will neglect the frequency dependence of the vertex, therefore we switch to letters as indices, each of which describes a lattice point with associated spin. The truncated unity approach we develop is analog to the k-space one. There, the main idea is that without inter-channel coupling the equations amount to a standard RPA series which will only produce a dependency on two spatial indices, or a single momentum (if the interaction is local). If we now include the coupling, we will technically generate dependencies on all indices, but the "native" ones will contain the main features. This indicates that only two orbital indices are of central importance and should be treated with high accuracy and for the others a lower accuracy is sufficient. We want to exploit this by an expansion of the two non-native indices in a basis centered at a native one. In a general real-space setting the basis is dependent on the position it is centered around, in contrast to the k-space form-factors [23]. Mathematically speaking we use a form-factor expansion of pairwise orthonormal functions which form a complete basis (see Eq. (4)):

$$\begin{aligned} \sum_i f_{b_k}(i) f_{b_k'}^*(i) &= \delta_{b_k, b_k'} \\ \sum_{b_k} f_{b_k}(i) f_{b_k}^*(i') &= \delta_{i, i'} \end{aligned} \quad (4)$$

Later the included form-factors in the unity are restricted to a small subset. We start with general form-factors for the derivation and specify them later on. With the usage of a basis we define the projections onto the main dependencies

of each channels in Eq. (5).

$$\begin{aligned}
\hat{P}[\Gamma]_{i,j}^{b_i,b_j} &= \Gamma(i, i + b_i; j, j + b_j) = \sum_{k,l} \Gamma(i, k; j, l) f_{b_i}(k) f_{b_j}^*(l) \\
\hat{C}[\Gamma]_{i,j}^{b_i,b_j} &= \Gamma(i, j + b_j; j, i + b_i) = \sum_{k,l} \Gamma(i, k; j, l) f_{b_i}(l) f_{b_j}^*(k) \\
\hat{D}[\Gamma]_{i,j}^{b_i,b_j} &= \Gamma(i, j + b_j; i + b_i, j) = \sum_{k,l} \Gamma(i, k; l, j) f_{b_i}(l) f_{b_j}^*(k)
\end{aligned} \tag{5}$$

This is exact and just a rewriting of the vertex as long as we do not truncate the basis. The full vertex can be recovered by a unprojection, the inverse projection, using the completeness relation in Eq. (4). Further we define the channels projected on their respective native indices in Eq. (6).

$$\begin{aligned}
P_{i,j}^{b_i,b_j} &= \hat{P}[\Phi^P]_{i,j}^{b_i,b_j} \\
C_{i,j}^{b_i,b_j} &= \hat{C}[\Phi^C]_{i,j}^{b_i,b_j} \\
D_{i,j}^{b_i,b_j} &= \hat{D}[\Phi^D]_{i,j}^{b_i,b_j}
\end{aligned} \tag{6}$$

Thus we recover the full vertex by applying

$$\Gamma = U + \hat{P}^{-1}[P] + \hat{C}^{-1}[C] + \hat{D}^{-1}[D]. \tag{7}$$

The flow equations for the projected channels can be derived from Eq. (3a)-(3c) with the help of an insertion of an unity, here shown exemplary for the P -channel

$$\frac{dP_{i,j}^{b_i,b_j}}{d\Lambda} = \sum_{k,l} \frac{d\Phi^P(i, k; j, l)}{d\Lambda} f_{b_i}(k) f_{b_j}^*(l) \tag{8}$$

$$\begin{aligned}
&= \sum_{k,l,i',k',j',l'} f_{b_i}(k) f_{b_j}^*(l) \Gamma(i, k; i', k') \sum_{n',m'} \delta_{n',k'}(G(i', j')S(n', m')) \delta_{m',l'} \Gamma(j', l'; j, l) \\
&= \sum_{k,l,i',k',j',l'} f_{b_i}(k) f_{b_j}^*(l) \Gamma(i, k; i', k') \sum_{b_{i'},n',b_{j'},m'} [f_{b_{i'}}(k') f_{b_{i'}}^*(n') (G(i', j')S(n', m')) \\
&\quad \times f_{b_{j'}}(l') f_{b_{j'}}^*(m') \Gamma(j', l'; j, l)]
\end{aligned} \tag{9}$$

$$\begin{aligned}
&= \sum_{b'_i,i',j',b'_j} \left[\sum_{k,k'} f_{b_i}(k) f_{b_{i'}}^*(k') \Gamma(i, k; i', k') \right] \left[\sum_{n',m'} f_{b_{i'}}(n') f_{b_{j'}}^*(m') (G(i', j')S(n', m')) \right] \\
&\quad \times \left[\sum_{l',l} f_{b_{j'}}(l') f_{b_j}^*(l) \Gamma(j', l'; j, l) \right]
\end{aligned} \tag{10}$$

$$= \sum_{b'_i,i',j',b'_j} \hat{P}[\Gamma]_{i,i'}^{b_i,b_{i'}} \chi_{pp(i',j')}^{b_{i'},b'_j} \hat{P}[\Gamma]_{j',j}^{b_{j'},b_j}. \tag{11}$$

The other equations can be derived analogously, resulting in the following coupled set of differential equations

$$\frac{dP_{i,j}^{b_i,b_j}}{d\Lambda} = \hat{P}[\Gamma]_{i,i'}^{b_i,b_{i'}} \chi_{pp(i',j')}^{b_{i'},b'_j} \hat{P}[\Gamma]_{j',j}^{b_{j'},b_j} \tag{12}$$

$$\frac{dC_{i,j}^{b_i,b_j}}{d\Lambda} = \hat{C}[\Gamma]_{i,i'}^{b_i,b_{i'}} \chi_{ph(i',j')}^{b_{i'},b'_j} \hat{C}[\Gamma]_{j',j}^{b_{j'},b_j} \tag{13}$$

$$\frac{dD_{i,j}^{b_i,b_j}}{d\Lambda} = \hat{D}[\Gamma]_{i,i'}^{b_i,b_{i'}} \chi_{ph(i',j')}^{b_{i'},b'_j} \hat{D}[\Gamma]_{j',j}^{b_{j'},b_j}, \tag{14}$$

where we defined the particle-particle and particle-hole propagator as

$$\chi_{pp(i',j')}^{b'_i,b'_j} = \sum_{n',m'} f_{b_{i'}}(n') f_{b_{j'}}^*(m') (G(i', j')S(n', m')) \tag{15}$$

$$\chi_{ph(i',j')}^{b'_i,b'_j} = \sum_{n',m'} f_{b_{i'}}(n') f_{b_{j'}}^*(m') (G(i', j')S(n', m') + S(i', j')G(n', m')). \tag{16}$$

The equations can be reinterpreted in terms of multi-index blockmatrix-products which are well optimized numerically.

As already mentioned we now want to truncate the basis expansion used in the derivation. This will in fact not change the projected flow equations, but it will change the vertex reconstruction as the inverse projection is not exact anymore. Therefore we obtain projections in between the three channels. The way how the basis is chosen as well as how it is truncated is not unique. The choice of a specific truncation can either be physically or systematically motivated. For example, the first one can be applied in Moiree-lattice models where we have two competing length scales. It is believed that such models can exhibit superconductivity at the scale of unit cell vectors which then could be included explicitly in the expansion. The second approach excludes contributions above a certain bond length or distance in a controlled manner. We can express this truncation as

$$\sum_{b_k \in L} f_{b_k}(i) f_{b_k}^*(i) = \sum_{b_k} \delta_{b_k}^L f_{b_k}(i) f_{b_k}^*(i) \approx 1, \quad (17)$$

where we defined the set of all allowed bonds L . We define $\delta_{b_k}^L$ to be one if $b_k \in L$ and zero otherwise. To obtain the explicit projections needed for the flow equations we now insert this into the full vertex projections and keep track of all occurring indices. Without specifying a specific basis or writing out spin dependencies, we obtain the general form of the projections

$$\hat{P}[\Gamma]_{i,j}^{b_i,b_j} = \hat{P} \left[U + \hat{P}^{-1}[P] + \hat{C}^{-1}[C] + \hat{D}^{-1}[D] \right]_{i,j}^{b_i,b_j} \quad (18)$$

$$\hat{C}[\Gamma]_{i,j}^{b_i,b_j} = \hat{C} \left[U + \hat{P}^{-1}[P] + \hat{C}^{-1}[C] + \hat{D}^{-1}[D] \right]_{i,j}^{b_i,b_j} \quad (19)$$

$$\hat{D}[\Gamma]_{i,j}^{b_i,b_j} = \hat{D} \left[U + \hat{P}^{-1}[P] + \hat{C}^{-1}[C] + \hat{D}^{-1}[D] \right]_{i,j}^{b_i,b_j}. \quad (20)$$

Before specifying our basis we take care of the spin degrees of freedom.

SU(2) symmetric formulation

To get rid off the spin degrees of freedom we will now assume that we have a $SU(2)$ -symmetric interaction and Hamiltonian, which allows to simplify the channels with the help of the crossing relations [28]

$$\begin{aligned} \Phi^P(ik; jl)_{\sigma_i \sigma_k \sigma_j \sigma_l} &= V^P(ki; jl) \delta_{\sigma_i \sigma_j} \delta_{\sigma_k \sigma_l} - V^P(ik; jl) \delta_{\sigma_i \sigma_l} \delta_{\sigma_k \sigma_j} \\ \Phi^C(ik; jl)_{\sigma_i \sigma_k \sigma_j \sigma_l} &= V^D(ki; jl) \delta_{\sigma_i \sigma_j} \delta_{\sigma_k \sigma_l} - V^C(ik; jl) \delta_{\sigma_i \sigma_l} \delta_{\sigma_k \sigma_j} \\ \Phi^D(ik; jl)_{\sigma_i \sigma_k \sigma_j \sigma_l} &= V^C(ki; jl) \delta_{\sigma_i \sigma_j} \delta_{\sigma_k \sigma_l} - V^D(ik; jl) \delta_{\sigma_i \sigma_l} \delta_{\sigma_k \sigma_j}. \end{aligned} \quad (21)$$

The spin degrees of freedom can now be eliminated by choosing a specific spin configuration. The full spin dependence can be reconstructed by applying the relations in Eq. (21). For the sake of simplicity we choose $(\sigma_i \sigma_k \sigma_j \sigma_l) = (\uparrow \downarrow \downarrow \uparrow)$ and redefine $P_{ij}^{b_i b_j} = V^P(i, i + b_i; j, j + b_j)$ and analogously for C and D . The diagrammatic flow equations now read

The diagrammatic equation shows a vertex with four external legs (two incoming, two outgoing) and a central shaded region. This vertex is equal to the sum of three channels: P^Λ , C^Λ , and D^Λ . P^Λ consists of two vertical legs and two horizontal legs. C^Λ consists of two vertical legs and two horizontal legs with a crossing. D^Λ consists of two vertical legs and two horizontal legs with a loop structure.

To write out the equations explicitly, we use Kronecker-deltas spanning the lattice around a specific site as a basis, defined as $f_{b_i}(k) = \delta_{i+b_i, k}$. We additionally assume a density-density type interaction. The sums in Eq. (12, 13, 14) can be reinterpreted as matrix-products in the multi-indices consisting of orbital and bond index. Thus, the flow

equations now simplify to

$$\begin{aligned}
\frac{dP}{d\Lambda} &= -\hat{P}[\Gamma] \cdot \dot{\chi}_{pp} \cdot \hat{P}[\Gamma] \\
\frac{dC}{d\Lambda} &= -\hat{C}[\Gamma] \cdot \dot{\chi}_{ph} \cdot \hat{C}[\Gamma] \\
\frac{dD}{d\Lambda} &= 2\hat{D}[\Gamma] \cdot \dot{\chi}_{ph} \cdot \hat{D}[\Gamma] \\
&\quad - \hat{C}[\Gamma] \cdot \dot{\chi}_{ph} \cdot \hat{D}[\Gamma] \\
&\quad - \hat{D}[\Gamma] \cdot \dot{\chi}_{ph} \cdot \hat{C}[\Gamma]
\end{aligned} \tag{22}$$

where $\dot{\chi}_{pp}$ and $\dot{\chi}_{ph}$ are redefined in terms of the spin summation. The Matsubara sum can be calculated either analytically which scales like $\mathcal{O}(N^4 N_b^4)$ (with N the number of orbitals) or numerically as a summation over the fermionic frequencies which scales proportional to $\mathcal{O}(N^3 N_b^2 N_f)$ (with N_f the number of frequencies and N_b the average number of bonds included). The number of frequencies can be reduced by taking a non-uniform Matsubara grid to approximately $10^2 - 10^3$ for reaching an accuracy below 10^{-5} at $T = 10^{-3}$, making the numerical approach faster than the semi-analytical. The required Greens-functions are precalculated and cached to reduce run-time. The propagators are given as

$$\dot{\chi}_{ph(i,j)}^{b_i, b_j} = 2 \sum_{\omega > 0} \Re(G(\omega)_{i,j} S(\omega)_{j+b_j, i+b_i} + G \leftrightarrow S) \tag{23}$$

$$\dot{\chi}_{pp(i,j)}^{b_i, b_j} = 2 \sum_{\omega > 0} \Re(G(\omega)_{i,j} S(-\omega)_{i+b_i, j+b_j} + G \leftrightarrow S). \tag{24}$$

The equation for the D -channel can be simplified by a completion of the square in its flow equations resulting in (defining $V_D = \hat{D}[\Gamma] - \frac{1}{2}\hat{C}[\Gamma]$)

$$\frac{dD}{d\Lambda} = 2V_D \dot{\chi}_{ph} V_D + \frac{1}{2} \frac{d}{d\Lambda} C \tag{25}$$

With the before defined Kronecker basis, the projections simplify due to the cancellation of sums. This results in Eq. (26)-(28) (compare to [26, 27]) introducing the difference set $\delta_{i,j}^d$ being one if the bond connecting i and j is included in the truncation.

$$\hat{P}[\Gamma]_{i,j}^{b_i, b_j} = P_{i,j}^{b_i, b_j} + \delta_{i,j+b_j}^d \delta_{i+b_i, j}^d C_{i,j}^{(j+b_j-i), (i+b_i-j)} + \delta_{i,j}^d \delta_{i+b_i, j+b_j}^d (D_{i,j+b_j}^{(j-i), (i+b_i-j-b_j)} + U_{i,j+b_j}^{(j-i), (i+b_i-j-b_j)}) \tag{26}$$

$$\hat{C}[\Gamma]_{i,j}^{b_i, b_j} = C_{i,j}^{b_i, b_j} + \delta_{i,j+b_j}^d \delta_{i+b_i, j}^d P_{i,j}^{(j+b_j-i), (i+b_i-j)} + \delta_{i,j}^d \delta_{i+b_i, j+b_j}^d (D_{i,i+b_i}^{(j-i), (j+b_j-i-b_i)} + U_{i,i+b_i}^{(j-i), (j+b_j-i-b_i)}) \tag{27}$$

$$\hat{D}[\Gamma]_{i,j}^{b_i, b_j} = D_{i,j}^{b_i, b_j} + \delta_{i,j+b_j}^d \delta_{i+b_i, j}^d P_{i,i+b_i}^{(j+b_j-i), (j-i-b_i)} + \delta_{i,j}^d \delta_{i+b_i, j+b_j}^d C_{i,i+b_i}^{(j-i), (j+b_j-i-b_i)} + U_{i,j}^{b_i, b_j}. \tag{28}$$

Decoupling of Vertex Function

At the final scale, we obtain an effective interaction for the low lying energy degrees of freedom, with which we can reformulate the Hamiltonian as:

$$H = H_0 - \frac{1}{4} \Gamma(\alpha, \beta; \gamma, \delta) \bar{\psi}_\alpha \bar{\psi}_\beta \psi_\gamma \psi_\delta \tag{29}$$

where we already went back to the Grassmann notation of the fermionic operators and introduced the multi-indices $\alpha = (i, \sigma_i)$. A post-FRG mean-field theory can enable a differentiation between competing orders, which are not separated by the FRG. But as the two approaches are decoupled, the resulting gap magnitudes depend on the stopping scale and should be therefore only be seen as qualitative ordering pattern. We now want to derive mean-field equations for the charge and spin gap. We restrict the derivation to a general, $SU(2)$ -symmetric vertex and rewrite the effective interaction in the channel decomposed form:

$$\Gamma(\alpha, \beta; \gamma, \delta) = U_{\alpha, \beta; \gamma, \delta} + \Phi^C(\alpha, \beta; \gamma, \delta) + \Phi^D(\alpha, \beta; \gamma, \delta)$$

where we neglected the pairing channel as for the cases in which we applied the mean-field decoupling it was suppressed with respect to the other channels. Additionally, we neglect the bare interaction, as in a flow to strong

coupling its influence is small and therefore negligible. In order to sum up the spin indices we again apply the relations (21). C and D are the channels we obtain as a result of our FRG scheme. We start with the Grassmann path integral for the partition function:

$$\mathcal{Z} = \int \mathcal{D}[\bar{\psi}, \psi] e^{S_0[\bar{\psi}, \psi]} \cdot e^{-\frac{1}{4} \bar{\psi}_\alpha \bar{\psi}_\beta \Phi^C(\alpha, \beta; \gamma, \delta) \psi_\gamma \psi_\delta} \cdot e^{-\frac{1}{4} \bar{\psi}_\alpha \bar{\psi}_\beta \Phi^D(\alpha, \beta; \gamma, \delta) \psi_\gamma \psi_\delta} \quad (30)$$

We now introduce a matrix notation for the vertex components without spin degrees of freedom:

$$I(j, k; i, l) = I_{i,j}^{l,k}$$

note that here we still have four spatial indices and no truncation has been applied yet. We will now write out the spin dependence explicitly using the relations Eq. (21)

$$\begin{aligned} \mathcal{Z} = \int \mathcal{D}[\bar{\psi}, \psi] e^{S_0[\bar{\psi}, \psi]} \cdot \exp \left[-\frac{1}{4} \bar{\psi}_j^{\sigma'} \bar{\psi}_k^\sigma C_{i,j}^{l,k} \psi_l^{\sigma'} \psi_i^\sigma + \frac{1}{4} \bar{\psi}_j^\sigma \bar{\psi}_k^{\sigma'} D_{l,j}^{i,k} \psi_l^{\sigma'} \psi_i^\sigma \right] \\ \cdot \exp \left[-\frac{1}{4} \bar{\psi}_j^{\sigma'} \bar{\psi}_k^\sigma D_{i,j}^{l,k} \psi_l^{\sigma'} \psi_i^\sigma + \frac{1}{4} \bar{\psi}_j^\sigma \bar{\psi}_k^{\sigma'} C_{l,j}^{i,k} \psi_l^{\sigma'} \psi_i^\sigma \right]. \end{aligned}$$

In order to have one type of index ordering per channel we commute the Grassmann variables and relabel the indices. The commutation of the fields results in an additional minus sign. We define the fermionic bilinears for each channel as:

$$\begin{aligned} C &\implies \chi_{i,j}^{\sigma, \sigma'} = \bar{\psi}_i^\sigma \psi_j^{\sigma'} \\ D &\implies \rho_{i,j}^{\sigma, \sigma'} = \bar{\psi}_i^\sigma \psi_j^{\sigma'} \delta_{\sigma\sigma'} \end{aligned}$$

Note that we have to use the physical channels in order to correctly assign all contributions to the respective mean-field. Those physical channels are defined as [51]

$$\begin{aligned} M_{i,j}^{l,k} &= \Phi^M(j, k; i, l) = -\Phi^C(j, k; i, l) \\ K_{i,j}^{l,k} &= \Phi^K(j, k; i, l) = 2\Phi^D(j, k; i, l) - \Phi^C(j, k; i, l). \end{aligned}$$

Φ^M defines the magnetic-channel, a divergence of it thus describes transitions to a magnetic phase. Φ^K describes the charge-channel indicating charge ordering. The charge-channel does not contain a spin divergence part anymore, unlike the D -channel. Thus if both channels, C and D , diverge the charge-channel does only contain the charge divergence which leads to an unambiguous decoupling.

Thereby the full $SU(2)$ -symmetric effective interaction is given as

$$\Gamma_{i,j}^{l,k} = -M_{i,j}^{l,k} + \frac{1}{2}(K_{i,j}^{l,k} - M_{i,j}^{l,k}).$$

Upon inserting and reordering of the terms we obtain:

$$\begin{aligned} \mathcal{Z} = \int \mathcal{D}[\bar{\psi}, \psi] e^{S_0[\bar{\psi}, \psi]} \cdot \exp \left[\frac{3}{4} M_{i,j}^{l,k} \bar{\chi}_{i,j}^{\sigma, \sigma'} \chi_{k,l}^{\sigma, \sigma'} \right] \\ \cdot \exp \left[-\frac{1}{4} K_{i,j}^{l,k} \bar{\rho}_{l,j}^{\sigma'} \rho_{k,i}^\sigma \right] \end{aligned}$$

For the decoupling we now introduce two bosonic fields using a Hubbard-Stratonovitch transformation [22]. In general this transformation reads (neglecting all occurring constants as we are only interested in the saddle point):

$$\exp \left[-\frac{1}{a} \bar{\eta}_m I_{m,n} \eta_m \right] = \int \mathcal{D}[\delta, \bar{\delta}] \exp \left[\frac{1}{q} \bar{\delta}_m I_{m,n} \delta_n - \frac{b}{q} \bar{\delta}_m I_{m,n} \eta_m - \frac{b}{q} \delta_n I_{m,n} \bar{\eta}_m \right] \quad (31)$$

With the restriction that $\frac{b^2}{q} = \frac{1}{a}$. We label the bosonic fields ϕ with the subscript of their respective channel, K for the charge-channel, M for the magnetic-channel. Additionally to the bosonic fields, we introduce the energy gap as condensation term, defined by $\Delta^I = I \circ \phi^I$ (\circ denotes a channel specific contraction of the tensor with the two fields, it will be specified later on, the charge gap contains an additional minus sign in its definition).

$$\begin{aligned}
\mathcal{Z} = & \int \mathcal{D}[\bar{\psi}, \psi] \mathcal{D}[\phi^M, \bar{\phi}^M] \mathcal{D}[\phi^K, \bar{\phi}^K] \\
& \cdot \exp \left[S_0[\bar{\psi}, \psi] + \frac{1}{2} \bar{\phi}_{k,l}^{M,\sigma,\sigma'} M_{i,j}^{l,k} \chi_{j,i}^{\sigma,\sigma'} - \frac{1}{2} \bar{\phi}_{j,l}^{K,\sigma} K_{i,j}^{l,k} \rho_{k,i}^{\sigma'} \right] \\
& \cdot \exp \left[\frac{1}{2} \phi_{k,l}^{M,\sigma,\sigma'} M_{i,j}^{l,k} \bar{\chi}_{j,i}^{\sigma,\sigma'} - \frac{1}{2} \phi_{j,l}^{K,\sigma} K_{i,j}^{l,k} \bar{\rho}_{k,i}^{\sigma'} + \frac{1}{3} \bar{\Delta}_{j,i}^M \phi_{k,l}^M - \bar{\Delta}_{j,l}^K \phi_{k,i}^K \right]
\end{aligned}$$

The fermionic part of the action is reduced to a Gaussian and thus integrable. In the absence of magnetic fields we assume that $\phi^M = \phi^{M,\uparrow\uparrow} = -\phi^{M,\downarrow\downarrow}$, $\phi^K = \phi^{K,\uparrow\uparrow} = \phi^{K,\downarrow\downarrow}$ and $\phi^{M,\uparrow\downarrow} = \bar{\phi}^{M,\downarrow\uparrow}$. Additionally, the diagonal gaps must be self-adjoint. To simplify the notation we introduce the Nambu spinor

$$\Psi_{\mathbf{i}} = (\psi_{\mathbf{i}}^{\uparrow} \quad \psi_{\mathbf{i}}^{\downarrow}), \quad (32)$$

with which we can rewrite the fermionic action in a compact form (note the reordering of Grassmann variables performed in order to have no minus signs occurring due to the integration):

$$\mathcal{Z}_f = \int \mathcal{D}[\bar{\psi}, \psi] \exp \left[\frac{1}{2} \bar{\Psi}_j (i\omega - \mathcal{M}_{ji}) \Psi_{\mathbf{i}} \right]$$

with the Matrix \mathcal{M} defined as

$$\mathcal{M} = \begin{pmatrix} H + \Delta^K + \Delta^M & \Delta^{M,\uparrow,\downarrow} \\ \bar{\Delta}^{M,\uparrow,\downarrow} & H + \Delta^K - \Delta^M \end{pmatrix}. \quad (33)$$

Here we assumed that the magnetic gap will break the spin rotational invariance. The gaps will be initialized as the leading eigenvectors of their respective relevant channel.

We now carry out the functional integrals, a Gaussian Grassmann integral, which results in (ignoring the prefactor as it has no effect on the saddle point equation)

$$\mathcal{Z}_f = \det(i\omega - \mathcal{M}) = \exp[\text{Tr}(\ln(i\omega - \mathcal{M}))] = \exp[\text{Tr}(\ln(G^{-1}))] \quad (34)$$

where we identified the Greens-function G . The mean-field equations are obtained by a saddle point approximation, defined as:

$$\frac{\delta \mathcal{Z}[\phi]}{\delta \phi} = 0 \iff \frac{\delta S[\phi]}{\delta \phi} = 0 \quad (35)$$

The variation of each field needs to vanish individually, leading to a coupled set of self-consistent equations. We sketch the derivation for the charge gap in the following (we suppress spin indices for brevity).

$$0 = \frac{\delta S[\phi^K, \bar{\phi}^K, \phi^{M,\sigma,\sigma'}, \bar{\phi}^{M,\sigma,\sigma'}]}{\delta \phi_{ij}^K} \quad (36)$$

$$= \text{Tr} \left(G_{mn} \cdot \frac{\delta G^{-1}[\phi^K, \bar{\phi}^K, \phi^{M,\sigma,\sigma'}, \bar{\phi}^{M,\sigma,\sigma'}]}{\delta \phi_{ij}^K} \right) - (\bar{\Delta}_{j,i}^K + \Delta_{j,i}^K) \quad (37)$$

$$= -2\Delta_{ij}^K - \sum_{\omega} \left(K_{n,j}^{i,m} (G(\omega)_{nm}^{\uparrow,\uparrow} + G(\omega)_{nm}^{\downarrow,\downarrow}) \right) \quad (38)$$

The spin indices are marking the spin block indices of the Greens-function. This equation can now be solved for the charge gap:

$$\Delta_{lj}^K = -\frac{1}{2} K_{i,j}^{l,k} \sum_{\omega} (G_{ik}^{\uparrow,\uparrow}(\omega) + G_{ik}^{\downarrow,\downarrow}(\omega)) \quad (39)$$

The equation for Δ^M follows analogously

$$\Delta_{ij}^{M,\sigma,\sigma'} = \frac{3}{2} M_{i,j}^{l,k} \sum_{\omega} (G_{lk}^{\sigma,\sigma'}(\omega) + (-1)^{\delta_{\sigma,\sigma'}} G_{lk}^{-\sigma,-\sigma'}(\omega)) \quad (40)$$

The channels we obtain from the TU calculation have the following index structure:

$$C(i, k; j, l) \rightarrow C(i, j + b_j; j, i + b_i) \quad (41)$$

$$D(i, k; l, j) \rightarrow D(i, j + b_j; i + b_i, j) \quad (42)$$

which leads to the following form of the physical channels

$$M_{i,k}^{b_i, b_k} = -\frac{3}{2} C_{i,k}^{b_i, b_k} \quad (43)$$

$$K_{i,k}^{b_i, b_k} = 2D_{i,k}^{b_i, b_k} - C_{i,k}^{b_i, b_k}. \quad (44)$$

We now return to the real-space TUFGR notation we introduced earlier, thus the index ordering is changed. Using the eigenvector-decomposition which we obtain as result of our FRG flow we reconstruct the approximate vertex as:

$$K(j, i + b_i; j + b_j, i) = K_{i,j}^{b_i, b_j} = \sum_k \lambda_k |k\rangle_i^{b_i} \langle k|_j^{b_j} \quad (45)$$

$$M(i + b_i, j; j + b_j, i) = C_{i,j}^{b_i, b_j} = -\sum_c \lambda_c |c\rangle_i^{b_i} \langle c|_j^{b_j} \quad (46)$$

This sum will be truncated to a few of the largest eigenvalue/eigenvector combinations indicated by a tilde from now on. Here we still need to sum out the inner spin index as well as the Matsubara sum. As the vertex is frequency independent this results in

$$\sum_{\omega} G_{kl} = \sum_n U_{kn} n_f(\lambda_n) U_{ln}^* = n_f(\mathcal{M})_{kl}. \quad (47)$$

The sum over all leading eigenvectors gives the effective channels resulting in the following set of self-consistent equations

$$\Delta_{i, i+b_i}^M = \frac{3}{2} \tilde{M}_{ij}^{b_i b_j} (n_f(\mathcal{M})^{\uparrow, \uparrow} - n_f(\mathcal{M})^{\downarrow, \downarrow})_{j, j+b_j} \quad (48)$$

$$\Delta_{i, i+b_i}^M = \frac{3}{2} \tilde{M}_{ij}^{b_i b_j} (n_f(\mathcal{M})^{\uparrow, \downarrow} + n_f(\mathcal{M})^{\downarrow, \uparrow})_{j, j+b_j} \quad (49)$$

$$\Delta_{i, i+b_i}^K = -\frac{1}{2} \tilde{K}_{ij}^{b_i b_j} (n_f(\mathcal{M})^{\uparrow, \uparrow} + n_f(\mathcal{M})^{\downarrow, \downarrow})_{j, j+b_j}. \quad (50)$$

If only a single channel is diverging, we can reduce the number of mean-fields to obtain a more efficient description. In practice we keep the particle number constant during the self-consistency iteration by adding an appropriate, adaptive chemical potential. We add and subtract the "zero gap charge gap" and absorb one part in this constant, the other part is used to redefine the charge gap

$$\tilde{\Delta}_{i, i+b_i}^K = \Delta_{i, i+b_i}^K - \Delta_{i, i+b_i}^K |_{\Delta^K=0} = -\frac{1}{2} \tilde{K}_{ij}^{b_i b_j} (n_f(\mathcal{M})^{\uparrow, \uparrow} + n_f(\mathcal{M})^{\downarrow, \downarrow} - \delta_{0, b_j} (n_f(H)^{\uparrow, \uparrow} + n_f(H)^{\downarrow, \downarrow}))_{j, j+b_j}. \quad (51)$$

The fixing of the particle number introduces convergence issues which are addressed by a mixing parameter (see Eq. (52)).

$$\Delta^{n+1} = \alpha \Delta^n + (1 - \alpha) \Delta^{n-1}. \quad (52)$$

Additionally, it introduces indirect coupling of the two regions, as particles cannot simply be pushed out of the one region. They then flow into the other region creating a charge displacement there. We always performed both simulations, once for fixed particle number and once for non-fixed particle number to check convergence. The non coupled MF/FRG leads to very large gap magnitudes which introduce additional convergence issues. This is resolved by a rescaling of the vertices by a factor, we used 1/10. As the resulting gap magnitudes are only qualitative this is not introducing a bias. In Fig. 5 we show the gap magnitudes for the non particle number fixed case of the coexistence of magnetic and charge ordering in the center Penrose model.

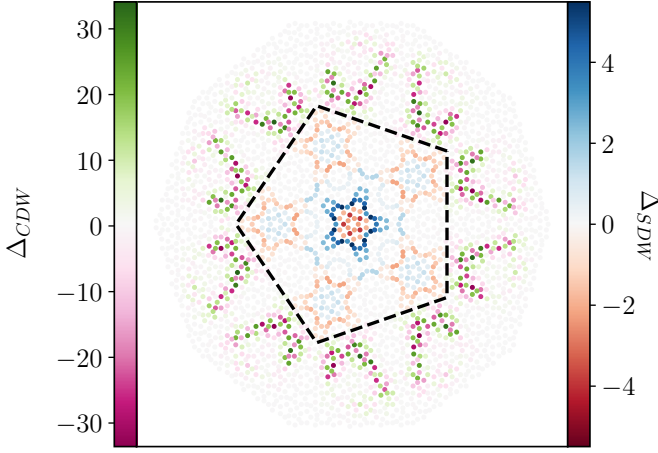


FIG. 5: Gap magnitudes of SDW and CDW in the center Penrose model at $\mu = 2.0$, $U = 0$, $U' = 0.3$ and $T = 10^{-3}$ without fixed particle number. It compares well to the gap predicted by the fixed particle number calculation. The calculated gap magnitudes are shown in a red-blue color scheme for the spin gap which is equivalent to the magnetisation. In the pink-green color scheme the charge gap is shown. The two faces have no spatial overlap of magnitudes above $10^{-3}\max(\Delta)$. The inserted dashed pentagon indicates the separation of spin and charge region.

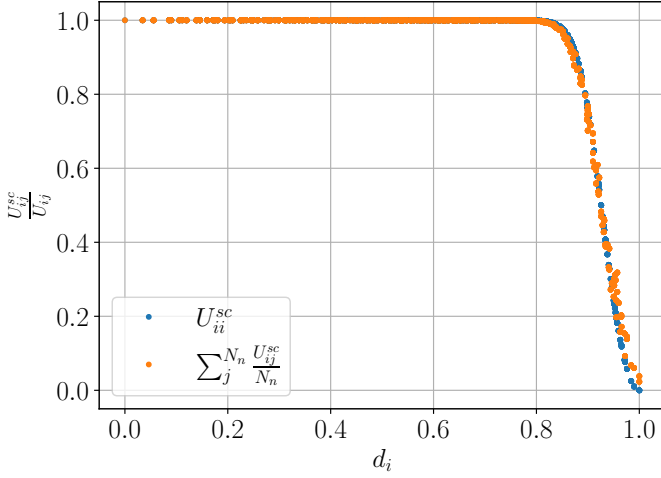


FIG. 6: Average on-site and nearest-neighbor interaction depending on the distance defined by the real-space positions to the center in the vertex-type Penrose model.

Screening of the interaction

For screening the interaction towards the boundaries we apply

$$U_{ii} \rightarrow U_{ii}^{sc} = U_{ii} \tanh(10 \cdot (d_{max} - d_i)^2) \quad (53)$$

as scaling factor for the interaction (d_i is the distance of site i to the center of the tiling and $d_{max} = \max_i d_i$). For the nearest-neighbor interactions, this factor is applied too. To keep the interaction symmetric and C^5 -invariant we need to symmetrize the scaling factor (see Eq. (54)) in, thereby we introduce a slight bias.

$$U_{ij}^{sc} = \frac{U_{ij}}{2} \cdot [\tanh(10 \cdot (d_{max} - d_i)^2) + \tanh(10 \cdot (d_{max} - d_j)^2)] \quad (54)$$

This creates a region of higher U'/U -ratio than in the bulk. This slight deviation seems not to have any influences as each interaction term is lower individually. The effective lattice size is of course reduced due to the application of the screening. The distance dependence of the screened on-site and nearest-neighbor interaction is shown in Fig. 6.

Non interacting Density of states

The non-interacting Density of states (DoS) has been calculated for the 9-times substituted lattice. We used the Kernel Polynomial Approximation method. The DoS was used in order to choose the parameters for the simulations. We focus on regions with high degeneracy or low slope of the dispersion relation in the diagonal basis of the Hamiltonian, both lead to strong peaks in the DoS.

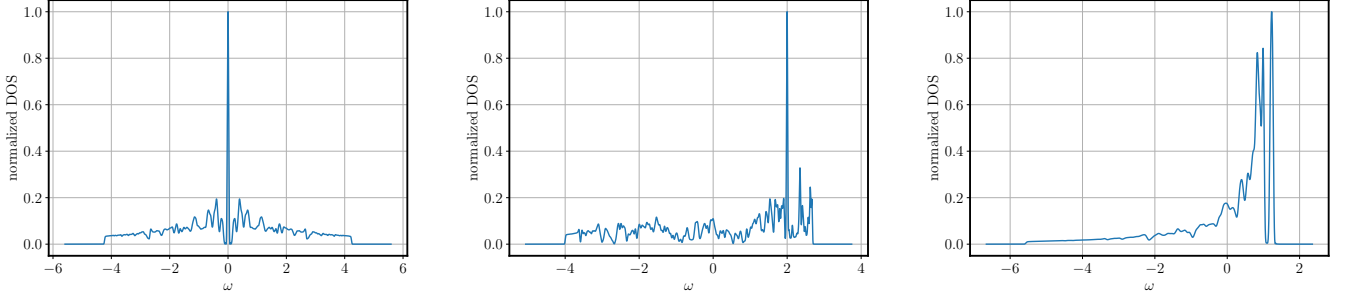


FIG. 7: Non interacting DoS for the three types of Penrose models used. Left, we have the vertex-type Penrose model with 21106 sites with the δ -like peak at $\mu = 0$. In the middle, we show the center-type model with hoppings defined using the graph, the main peak is at $\mu = 2.0$. On the right, we show the center-type model with exponential decaying hoppings, with three main peaks. In both center type models the lattice contains 20800 sites.

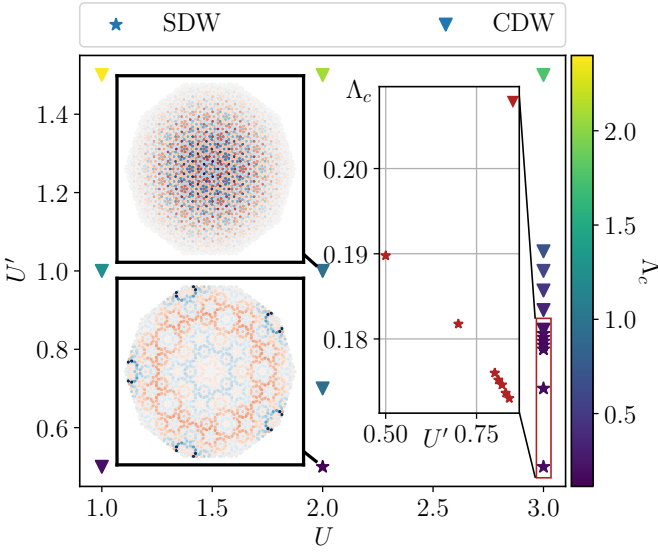


FIG. 8: Critical scales of CDW and SDW divergences at $\mu = 0.0$ and $T = 10^{-3}$. Upper left inset shows the charge order at $U' = 1.5$ and $U = 1$, the colormap is diverging so blue and red mark different signs. The lower left inset shows the spin order parameter (or magnetization pattern), at $U' = 0.5$ and $U = 2.0$. On the right side, the critical scales depending on the nearest-neighbor interaction are shown for $U = 3.0$ to highlight the suppression of the critical scale upon approaching the phase transition.

Non-screened Vertex model at half filling

For the non-screened interaction, the main results are summarized in Fig. 8. We find a charge-density wave phase at dominant nearest-neighbor interactions (U') and a spin-density wave phase at dominant on-site interactions. The latter is expected as in the limit of weak U' we should recover the known antiferromagnet for the vertex model. The SDW phase has its main weight at the boundaries, which is a consequence of the open boundary conditions and can be understood as follows. At the boundaries the local kinetic energy bandwidth is reduced, which results in a larger U/w_D ratio, which in term leads to faster divergences of diagrammatic re-summations at the boundaries. The sub-leading eigenvectors of the SDW divergence also show this bulk behavior. Upon decreasing U' , this effect is also vanishing as it should be. The CDW phase loses weight towards the boundaries and thus is seen as a bulk phase. Due to the reduced boundary weight, it could be possible that a coexisting boundary phase emerges at lower critical scales or lower temperatures. However, we did not find a phase coexistence. At the transition between CDW and SDW we find a mutual suppression of the phases resulting from their non-zero overlap in space.

This behavior can be understood as follows. In a C -channel (SDW) antiferromagnetic divergence the D -channel (CDW) has an eigenvalue, describing the strength of the order, half as large as the one of the C -channel, which already follows from the RPA. This eigenvalue is in our sign convention positive. The diverging eigenvalue of the CDW-RPA itself is negative, thus the two will suppress each other in the vertex reconstruction. This partial cancellation is the source of the reduced critical scales and thus reduced transition temperatures. As soon as the CDW divergence is dominant the critical scales grow rapidly again, as shown in the right inset of Fig. 8.

Phase-diagram of the center model at different fillings.

In Fig. 9 the dependence of the ordering on μ , U and U' is summarized for the center model. We find that non-localized divergences only occur in the vicinity of the main divergence. For all data sets we found more than a single diverging eigenvalue, thus more than a single channel mean-field decoupling is performed to extract the ordering information.

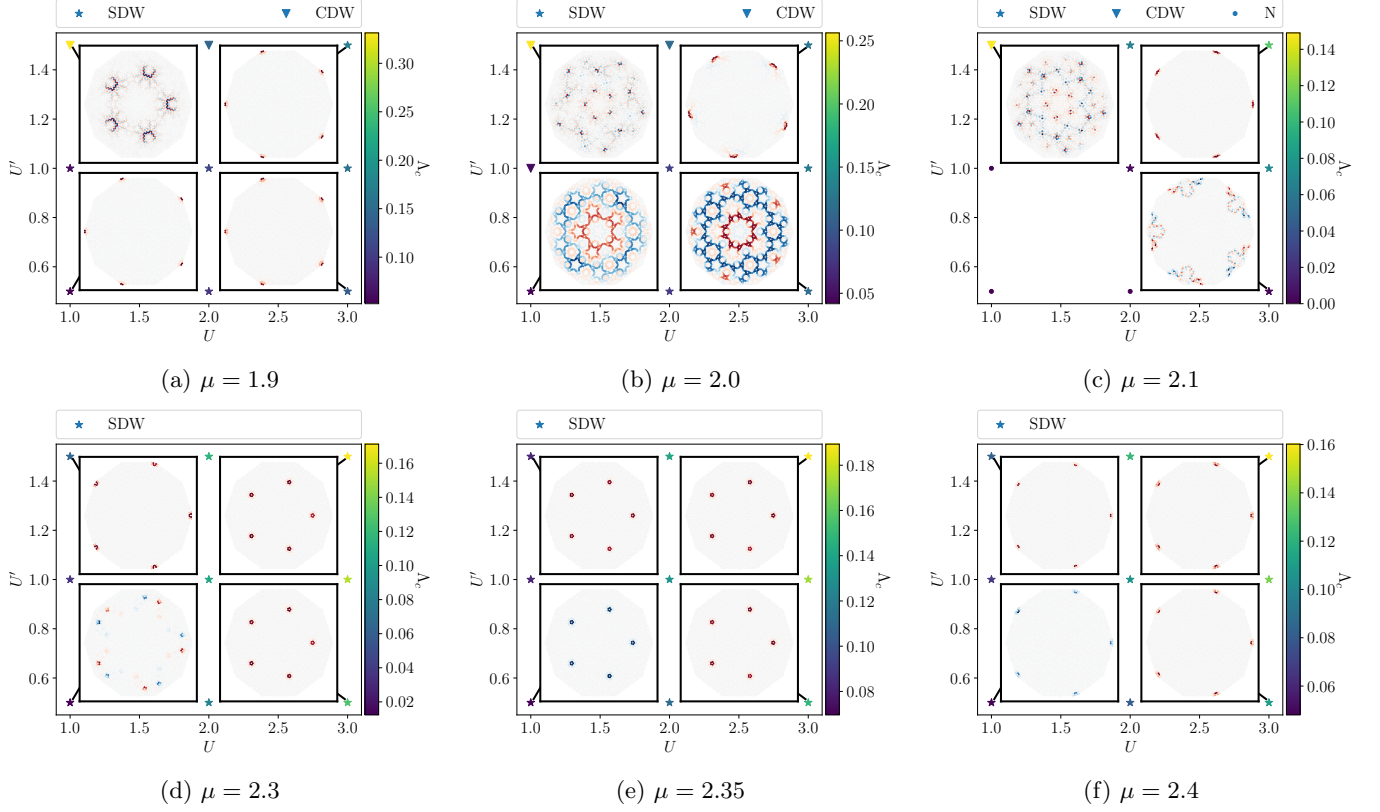


FIG. 9: Phase-diagram of the center model at different chemical potentials with ordering predictions from post-production mean field theory at chosen data points. U and U' are varied at $T = 10^{-3}$, nearest neighbors are included in the calculation. The colormap is diverging thus blue and red mark different signs, we normalized the gap to ± 1 .

Phase-diagram exponential hopping center model at different fillings.

For the exponential hopping center model we find the interaction dependence of the critical scale as summarized in Fig. 10. A clear classification in standard categories like AFM and FM is not possible thus we just state that SDW indicates a magnetic ordering. For each filling we display examples of the SDW ordering at the lowest and highest interaction strength in Fig. 11.

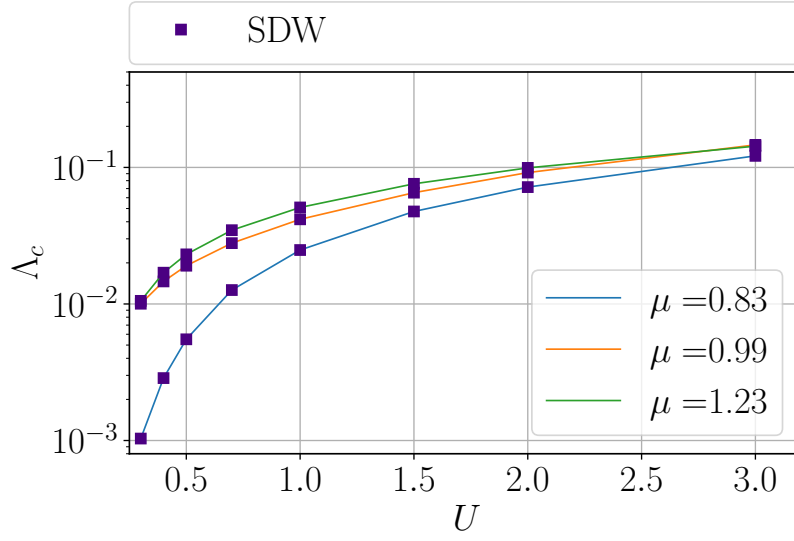


FIG. 10: Critical scales depending on the interaction strength in the center model with exponential hoppings at $T = 10^{-3}$ including all sites with a distance $\leq 3a$ in the calculation.

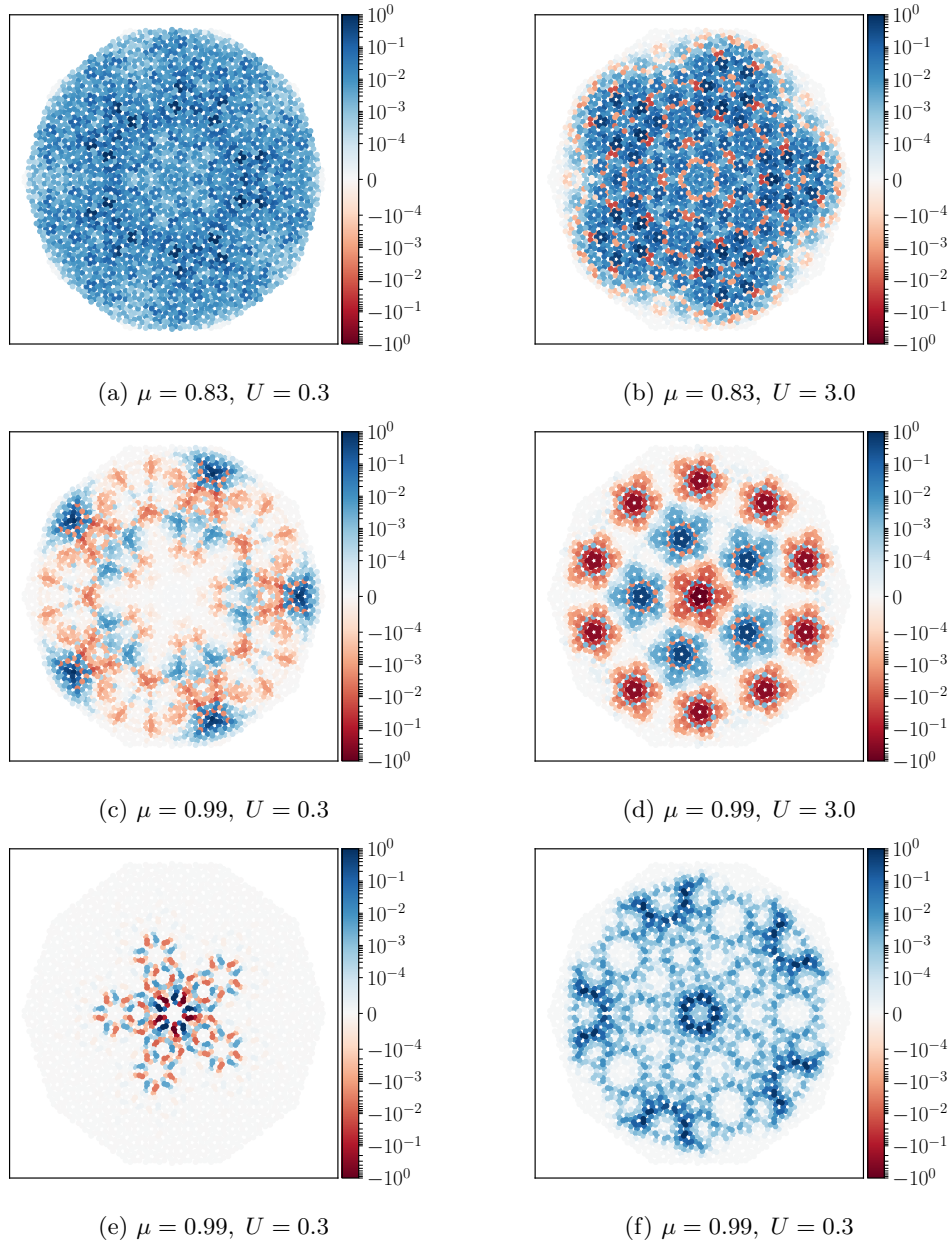


FIG. 11: Orderings at varying chemical potentials and interaction strength for the physical center model. Calculations are performed at $T = 10^{-3}$ using a frequency-cutoff including all sites with a distance $\leq 3a$ in the calculation. The colormap is diverging thus blue and red mark different signs, we normalized the gap to ± 1 and applied a logarithmic scale.